Supplementary Information (SI) for Lab on a Chip.
This journal is © The Royal Society of Chemistry 2025

Supporting Information

Leveraging dielectrophoresis in inertial flows for versatile manipulation of micro and nanoparticles

Haotian Cha[a], Lingxi Ouyang[a], Xiangxun Chen[a,b], Yuao Wu[a], Xiaoyue Kang[c], Hongjie An[a,d], Weihua Li[e], Nam-Trung Nguyen*[a], Jun Zhang[*a,f]

[a] Queensland Micro- and Nanotechnology Centre, Griffith University, Nathan, Queensland 4111, Australia. E-mail: jun.zhang@griffith.edu.au; nam-trung.nguyen@griffith.edu.au

[b] Bioscience Discipline, School of Environment and Science, Griffith University, Nathan, Queensland 4111, Australia

[c] School of Mechanical and Mining Engineering, The University of Queensland, Brisbane, QLD 4072, Australia.

[d] School of Environment Science, Griffith University, 170 Kessel Road, Nathan, QLD 4111, Australia

[e] School of Mechanical, Materials, Mechatronic and Biomedical Engineering, University of Wollongong, Wollongong, 2522 Australia

[f] School of Engineering and Built Environment, Griffith University, Brisbane, QLD 4111, Australia

To whom correspondence may be addressed:

*Jun Zhang; **Email:** jun.zhang@griffith.edu.au;

Table of Contents

S1 Supporting Information for Theoretical analysis of coupling DEP force and inertial lift forces

S1.1 Inertial Migration

In a Newtonian fluid environment, the dispersed particles will migrate laterally to unique cross-sectional equilibrium positions due to competition of the two inertial lift forces – shear gradient lift force F_{LS} and wall lift force F_{LW}.[1-3] The shear-gradient-lift force F_{LS} results from the curvature of the fluid velocity profiles, directing the particles to the channel walls. The wall lift force F_{LW} comes from the disturbance of the flow field around the particles near channel walls, pushing the particles away from the channel wall.[4] Based on the assumption that particle size is much smaller than the channel dimension, the net inertial-lift force F_L is expressed as:[1]

$$F_L = \frac{\rho U^2 a^4}{{D_h}^2} f_L \#(S1)$$

where a is the particle diameter and f_L is the dimensionless coefficient of inertial-lift force, which is a function of the particle size, cross-sectional position, and Reynolds number. ρ is the fluid density. U is the average flow velocity, and D_h is the channel hydraulic diameter.

The recent work of Zhou and Papautsky [5] indicates that: $f_L \propto a^{-2} U^{-0.5}$. Therefore $F_L \propto \frac{\rho U^{1.5} a^2}{{D_h}^2}$.

S1.2 Secondary flow in curved channels

In a curved channel, an additional inertial effect — secondary flow, a minor flow perpendicular to the main flow—is generated and applied to the particles.[3, 6] Fluids near the centre with larger inertial momentum tend to flow outwards around the curved region, pushing the fluids near the wall to move inward along the circumference. This results in two counter-rotating streamlines in the cross-sections of channels, also termed Dean vortices.[1, 7, 8] The average magnitude of the Dean flow velocity scales as[7]

$$U_D \sim \frac{De^2 v}{D_h} \#(S2)$$

where $v = \mu/\rho$ is the kinematic viscosity of the fluid. The dimensionless Dean number De describes the average strength of Dean flow, which can be expressed as [4]

$$De = \sqrt{\frac{D_h}{2R}}Re \#(S3)$$

where R represents the radius of the channel curvature. The Dean flow applies a drag force on particles to pull particles to follow the streamline. Assuming that the particles are kept stationary in the channel cross section, based on the Stokes law, the magnitude of the Dean drag force, F_D, can scale as[8]

$$F_D \sim \frac{\mu^2 a De^2}{\rho D_h} \#(S4)$$

The counterbalance of inertial lift and Dean drag forces will determine the final particle focusing positions in a curved channel.[8, 9] The relative ratio between inertial lift and Dean drag forces scales as:[10]

$$\frac{F_L}{F_D} \sim \frac{Re^2}{De^2}\left(\frac{a}{D_h}\right)^3 f_L = \frac{2Ra^3}{D_h^4} f_L \#(S5)$$

Generally, the inertial lift forces tend to retain the particles at the inertial equilibrium positions. In contrast, the Dean drag force is prone to drag particles to follow the counter-rotating streamlines. Under limiting conditions, when inertial lift force becomes dominant, $F_L >> F_D$, particles migrate to inertial equilibrium positions independent of the secondary flow. When $F_L << F_D$, Dean drag force dominates, particles follow the rotating secondary flow streamlines. In the intermediate range where F_L and F_D are in a similar order of magnitude, the secondary flow modifies the inertial equilibrium positions.[1]

Previous studies mostly modified inertial focusing positions by optimising channel geometry and dimensions or adjusting fluid flow rates. In this work, a new mechanism is proposed, which is coupling DEP forces along the vertical direction. The vertical locations of particles can be finely controlled by DEP forces. Because secondary flow distribution is not uniform but depends on the vertical distance (due to the wall boundary effects), the strength and direction of secondary flow drag on particles can be modified. Subsequently, the lateral migration and final focusing positions of particles in three dimensions (3D) can be delicately controlled.

S1.3 Dielectrophoresis

Dielectrophoresis (DEP) is the migration of particles in a non-uniform electric field. This force arises from the interaction between the field-induced electric polarisation of particles and the non-uniform electric field. [11] Under an alternating electric field, the time-averaged DEP force is expressed as [12, 13]

$$F_{Dep} = 2\pi\varepsilon_m r^3 Re[K(\omega)]\nabla|E_{rms}|^2 \#(S6)$$

where, ε_m is the permittivity of the suspending medium; r presents the radius of a spherical particle; E_{rms} is the root-mean-squared value of the applied electrical field; Re [K(ω)] is the real part of the Clausius–Mossotti (CM) factor. The CM factor is defined as:[11, 14]

$$K(\omega) = \frac{{\varepsilon_p}^* - {\varepsilon_m}^*}{{\varepsilon_p}^* + 2{\varepsilon_m}^*}, \#(S7)$$

$${\varepsilon_p}^* = \varepsilon_p - \frac{i\sigma_p}{\omega}, \#(S8)$$

$${\varepsilon_m}^* = \varepsilon_m - \frac{i\sigma_m}{\omega}, \#(S9)$$

where, ${\varepsilon_p}^*$ and ${\varepsilon_m}^*$ are the complex permittivity of the particle and medium, respectively. ε_p, σ_p and σ_m are the permittivity and conductivity of the particle and conductivity of the medium, respectively. ω is the angular frequency of the electric field.

The Clausius-Mossotti (CM) factor determines the direction of the force on particles. When the CM factor is positive (Re [K(ω)] > 0), indicating that the particles or cells have higher permittivity or conductivity than the solution, a positive DEP (p-DEP) force attracts them to regions of higher electric field gradient. Conversely, if the particles or cells have a lower polarization than the medium, the CM factor is negative (Re [K(ω)] < 0), causing a negative DEP (n-DEP) force that pushes them towards regions of lower electric field strength.

The value of the CM factor determines the direction of the force on particles. When the CM factor is positive (Re [K(ω)]>0), the permittivity or conductivity of particles/cells is greater than that of the solution, positive DEP (p-DEP) force attracts particles/cells to the stronger electric field. Conversely, if the polarization of particles/cells is lower than the medium, the CM factor is negative (Re [K(ω)]<0), causing a negative DEP (n-DEP) force to push particles towards regions of lower electric field strength.[15-17]

S1.4 Physical coupling of DEP and inertial lift forces

The symmetric IDE layers on the top and bottom layers enable the physical coupling of DEP and inertial lift forces at the inertial flow region. The ratio of DEP force to inertial lift force is given by:

$$\frac{F_{DEP}}{F_L} = \frac{\pi\varepsilon_m Re[K(\omega)]\nabla|E_{rms}|^2 {D_h}^2}{4\rho U^2 a f_L} \propto \frac{a\ Re[K(\omega)]}{U^{1.5}} \#(S10)$$

In this work, we investigated the coupling of both p-DEP and n-DEP forces with inertial flows to manipulate and separate particles and cells. For polystyrene particles suspended in DI water, the calculated CM factor curve is shown in Fig. S4. At the experimental electric frequency of 1 MHz, the CM factor was approximately -0.5, and the n-DEP forces repel particles off the electrode layers. Equ (S11) indicates that particles with a larger size will be pushed further away from the electrodes and closer to the channel vertical centre than the smaller ones. Consequently, secondary flow can amplify the lateral displacement of particles based on a minor difference along the vertical direction, which facilitates particle size-based separation.

Besides, viable and nonviable cells have different dielectric properties due to changes in their cellular structure and composition during cell death, such as changes in cell membrane properties and intracellular composition.[18] Therefore, the dielectric spectra of live and dead CHO cells are different, Fig. 3B. At 1 MHz, dead and live CHO cells experience distinct n-DEP and p-DEP forces, respectively. They are respectively repelled off and attracted toward the electrode layers. This difference in the vertical displacement is reflected and amplified in the lateral positions of particles by the secondary flow. This enables the dielectric property-based separation of cells.

S1.5 Numerical simulation

We numerically simulated the electric field of the interdigitated electrode by using COMSOL Multiphysics 6.0 software. In this process, the AC module was applied to a 2D geometry model that has the electrode dimension. The DEP force was calculated using the formula S6. In the electric field simulation result, the arrow vectors represent the magnitude and direction of the n-DEP or p-DEP forces. The background colour map illustrates the electric field distribution. The bulk conductivity and permittivity of the polystyrene beads are 2.4×10^{-4} S/m and $2.6\varepsilon_o$, respectively. The conductivity and permittivity of DI water are 1.5×10^{-4} S/m and $78\varepsilon_o$, respectively. The vacuum permittivity $\varepsilon_0 = 8.854187817\times10^{-12}$ F/m, and the particle size is 10 μm. When calculating the n-DEP force, Re[K(ω)] is approximated as -0.5, based on polystyrene particles in DI water at an electric frequency of 1 MHz, as shown in SI Appendix Fig. S4. The value of the p-DEP force has the opposite value of the n-DEP force. To account for different alignment conditions in the experiment, we simulated the electric field under both matched and staggered interdigitated electrode (IDE) layouts, as shown in the SI Appendix, Figures S2 and S3. The simulation results indicate that, despite differences in electrode layout, there is no significant variation in the magnitude or direction of DEP forces, and the DEP force distribution remains symmetric along the vertical center of the channel. Furthermore, for different gaps between the top and bottom electrodes, the oscillation direction of DEP forces remains consistent across both layouts, although the magnitude of the DEP force is slightly higher at lower heights, as observed in SI Appendix, Figures S2 and S3.

Fig. S1. Fabrication process of DEP-inertial microfluidic devices.

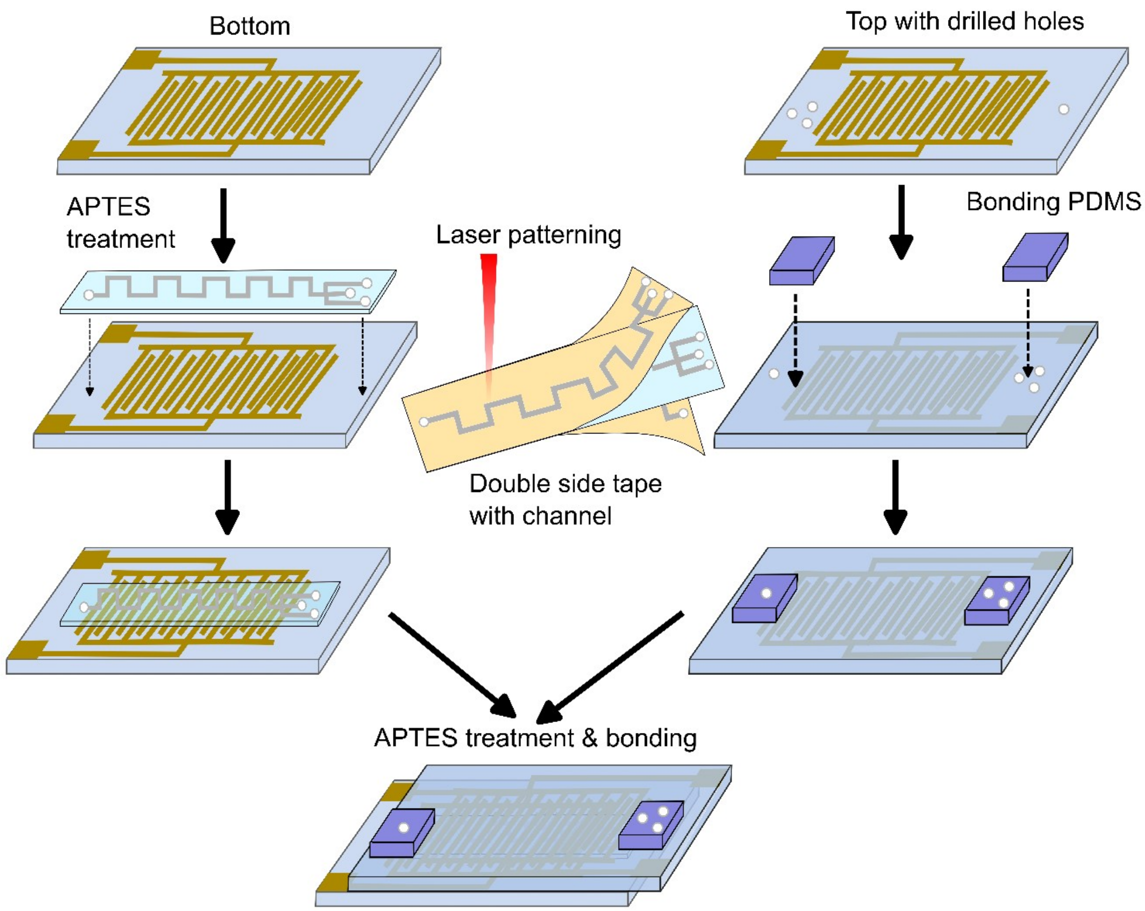

Fig. S1. Fabrication process of DEP-inertial microfluidic devices. The hybrid DEP-inertial microfluidic device consists of three layers: the top and bottom electrode layers and the middle fluidic channel layer.

Fig. S2. Simulation results of electric field and DEP forces with channel height (H) of 50 μm

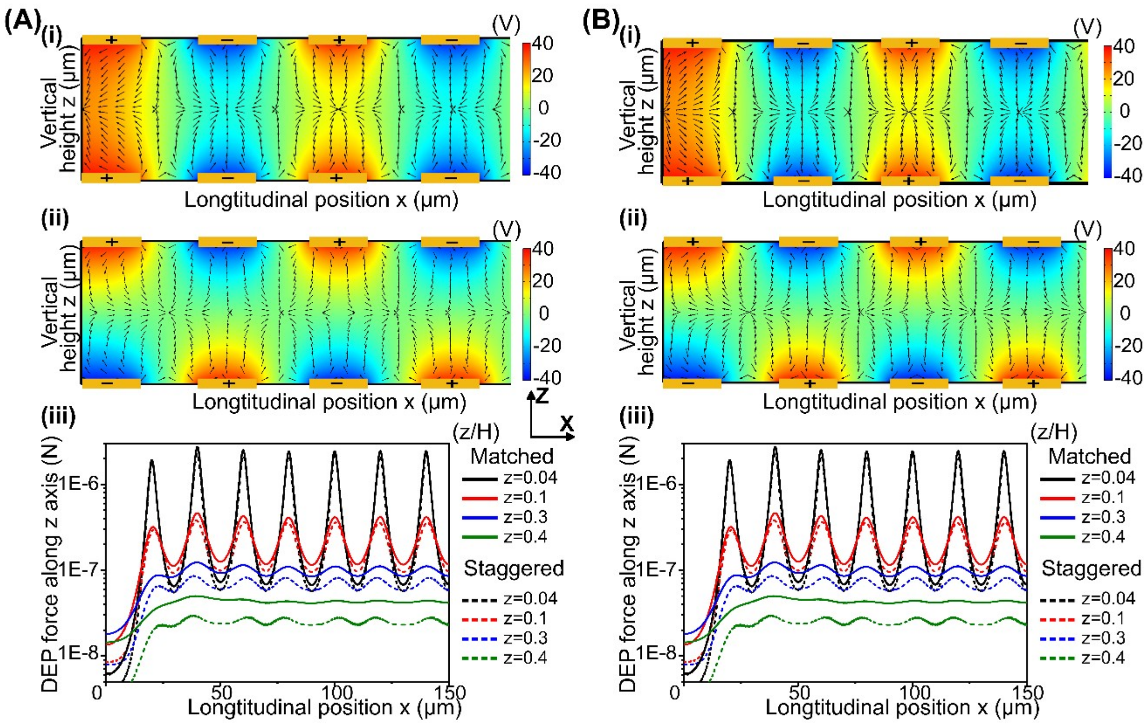

Fig. S2. Simulation results of electric field and DEP forces with channel height (H) of 50 μm. (A) The n-DEP force distribution under matched and staggered IDE electrode layout with a height (H) of 50 μm. The distribution of electric field and n-DEP force for the (i) matched and (ii) staggered electrode layout. (iii) Longitudinal distribution of the vertical n-DEP force (F_{DEPz}) between matched and staggered electrode layout. (B) The p-DEP force distribution under matched and staggered IDE electrode layout with height (H) of 50 μm. The distribution of electrical field and p-DEP force for the (i) matched and (ii) staggered electrode layout. (iii) Longitudinal distribution of the vertical p-DEP force (F_{DEPz}) between matched and staggered electrode layout. There is no significant difference in the magnitude and direction of DEP forces in both electrode layouts, where the DEP force distribution remains symmetric along the vertical centre of the channel. Moreover, for the force distribution in n-DEP and p-DEP, the only difference is the direction of the force, where the p-DEP force pointed to the electrode layers while the n-DEP force pointed to the centre of the channe.

Fig. S3 Simulation results of electrical field and DEP forces with channel height (H) of 30 μm

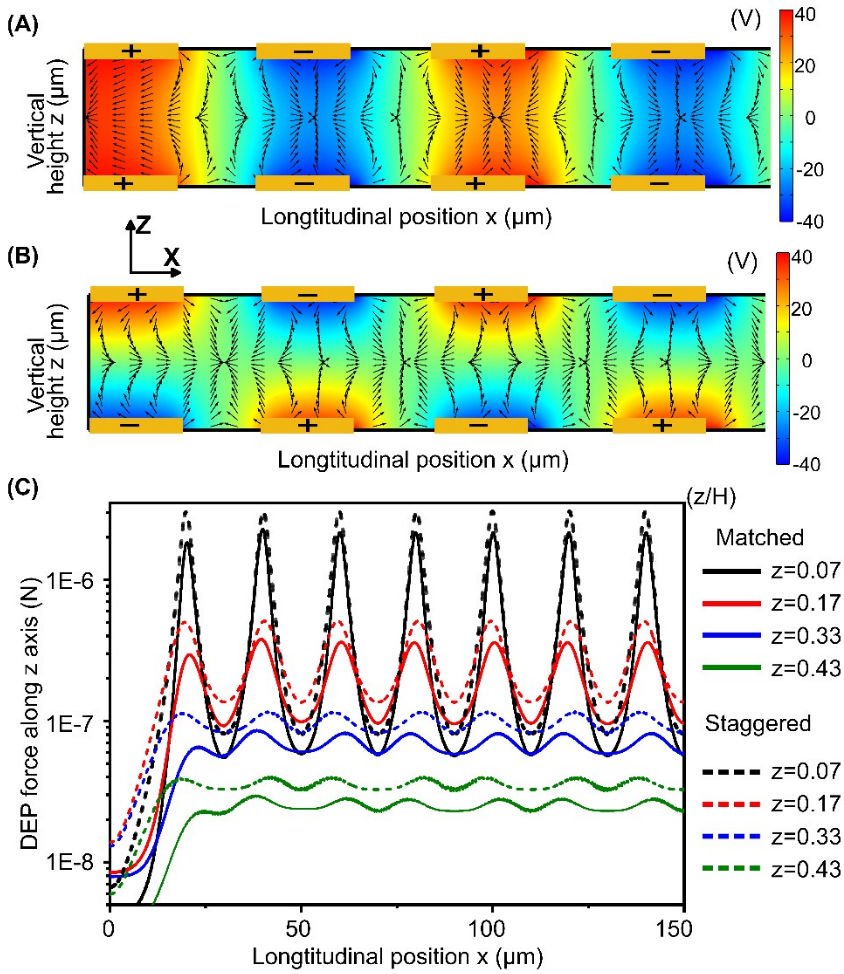

Fig. S3. The n-DEP force distribution under staggered IDE electrode layout with height (H) of 30 μm. (A) The distribution of electric field and n-DEP force for the (A) matched and (B)staggered electrode layout. (C) Longitudinal distribution of the vertical n-DEP force (F_{DEPz}) between matched and staggered electrode layout. There is a similar oscillation direction for both electrode layouts, while the magnitude of DEP force in staggered layouts is slightly higher than the matched one.

Fig. S4 CM factor curve of 10 μm particles in DI water

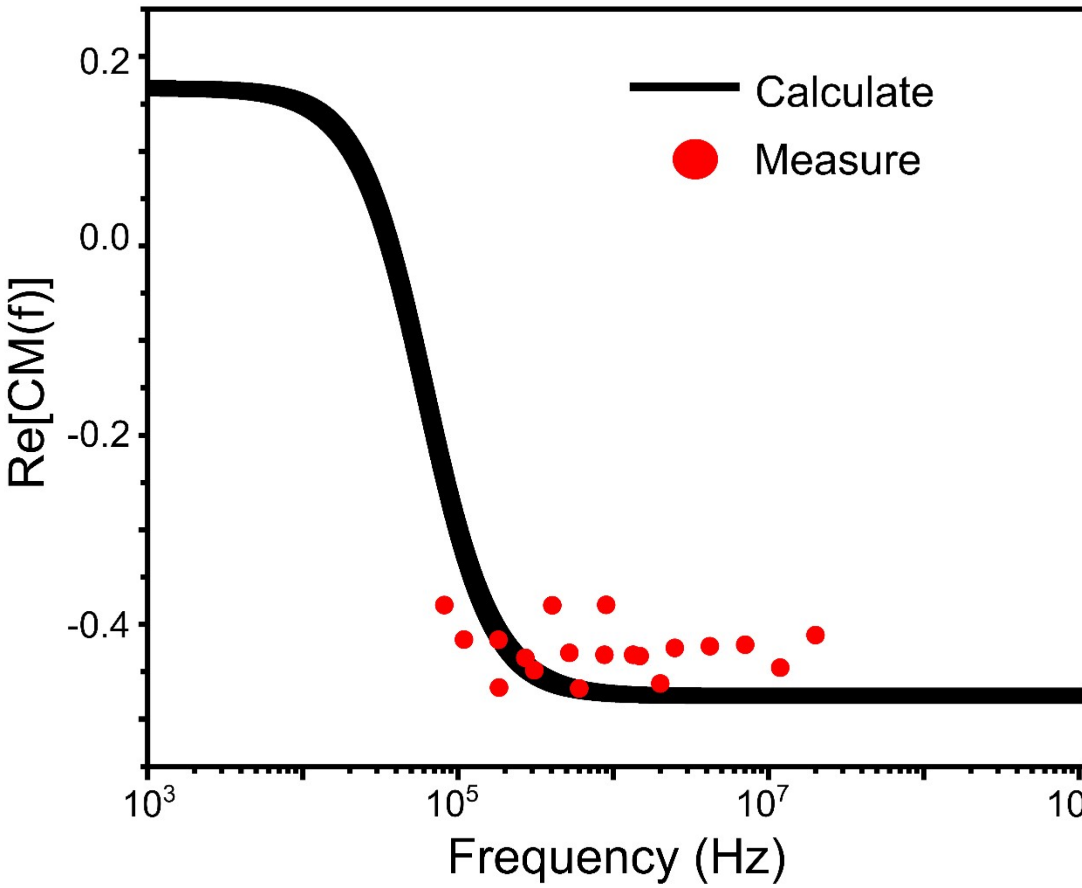

Fig. S4. The CM factor curve of 10 μm particles in DI water. The calculated theoretical Clausius-Mossotti (CM) factor of 10 μm particles in DI water under different electric frequencies is illustrated in Fig. S1. The bulk conductivity and permittivity of the polystyrene beads are 2.4×10^{-4} S/m and $2.6\varepsilon_o$, respectively. The conductivity and permittivity of DI water are 1.5×10^{-4} S/m and $78\varepsilon_o$, respectively. [19] The vacuum permittivity $\varepsilon_0 = 8.854187817 \times 10^{-12}$ F/m.

Fig. S5 Particle focusing positions in a DEP-serpentine channel under various electric voltages.

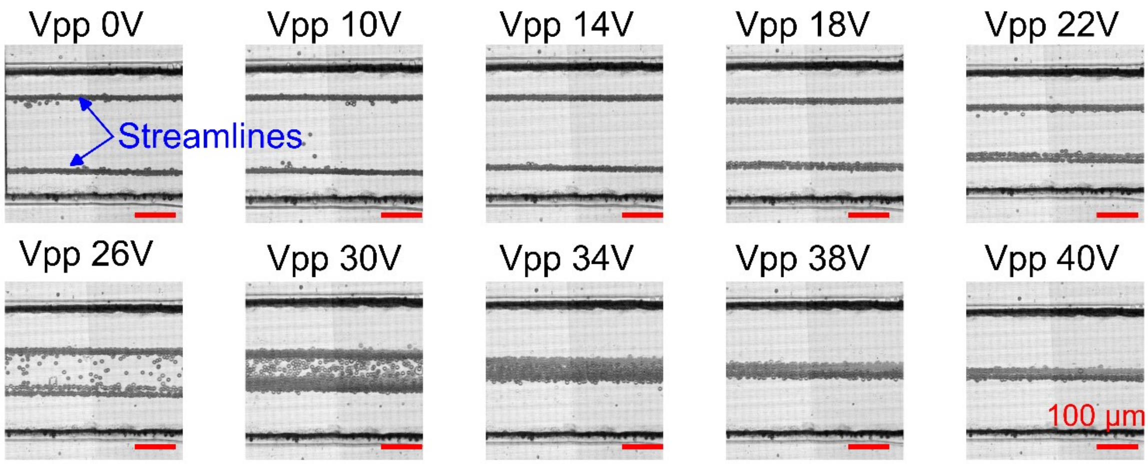

Fig. S5. The particle focusing positions in a DEP-serpentine channel under various electrical voltages. The flow rate is 500 µL/min (Re = 47) and the particle size is 10 µm. Particles focus on two symmetric equilibriums near the sidewalls before applying the electric field. When n-DEP forces repel particles off the electrodes, particles migrate toward the channel centre along the lateral direction. Two-sided focusing streaks can even combine as a single central one when the electric voltage is above a threshold. All images of particle focusing positions are stacked after being captured with a high-speed camera under a microscope.

Fig. S6 Particle focusing positions in a DEP-spiral channel under various electric voltages

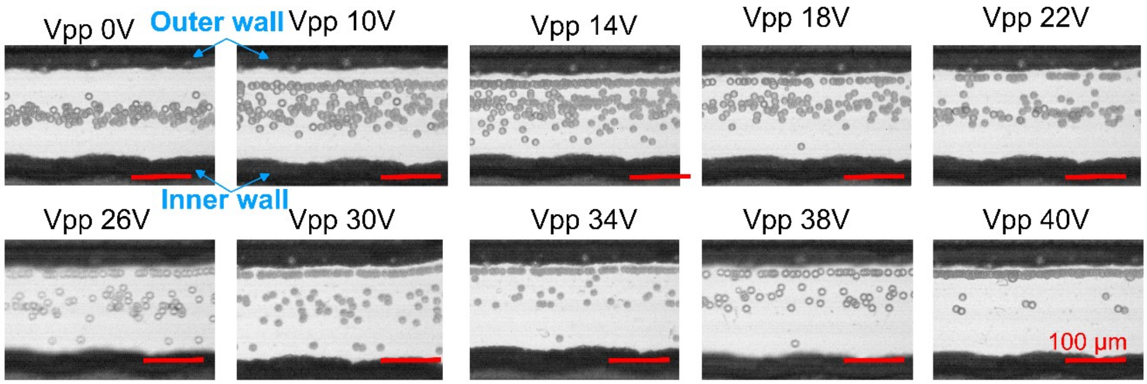

Fig. S6. The particle focusing positions in a DEP-spiral channel under various electric voltages. The flow rate is 100 μL/min (Re = *18*), and the particle size is 10 μm. When n-DEP forces repel particles off the electrodes, particles migrate toward the outer wall. When the electrical voltage is above a threshold voltage, the particles will migrate toward the outer wall region, combining a single streamline. All images of particle focusing positions are stacked after being captured with a high-speed camera under a microscope.

Fig. S7 Full-scale of images of culture wells at 4- and 24-hour post-seeding.

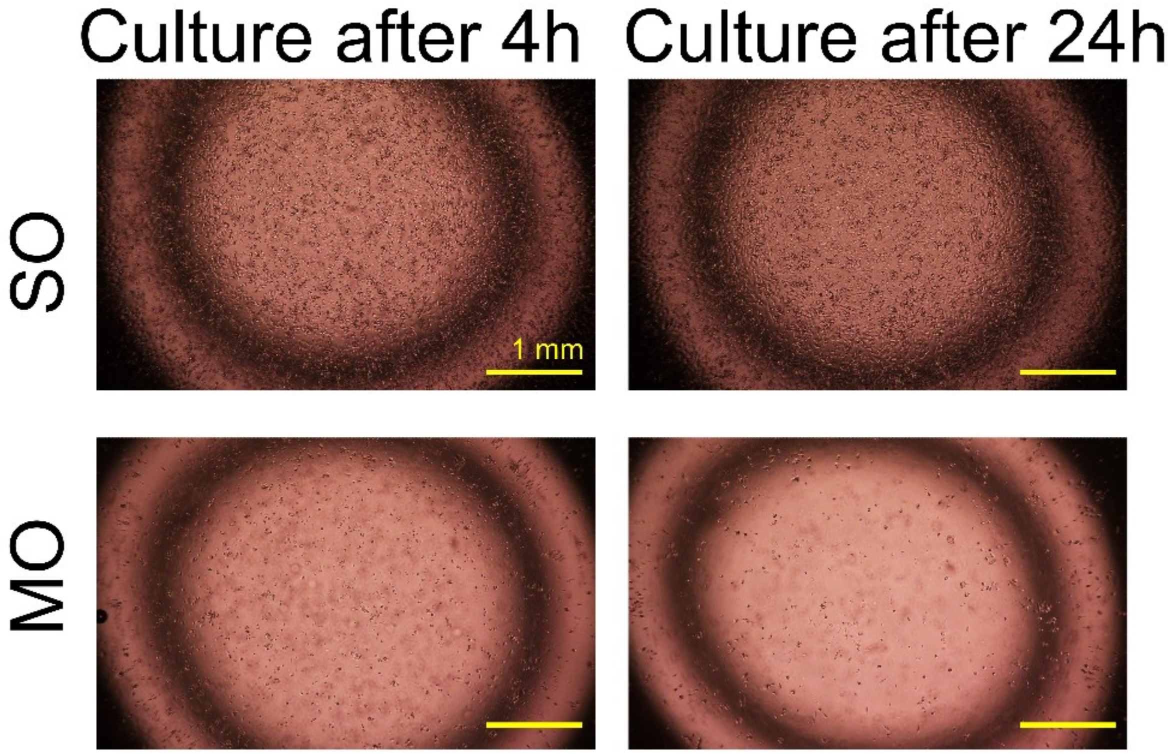

Fig. S7. Full-scale images of the culture wells at 4- and 24-hour post-seeding (with samples diluted ×4). The results show that cells from side outlets (SO) grew well, with increased attachment and proliferation over time, almost covering the entire culture well. In the middle out (MO) culture well, the number of cells was lower compared to the initial state, as dead cells were unable to attach and proliferate.

Fig. S8 Effect of the electric voltage on focusing 500-nm particles in a DEP-spiral channel

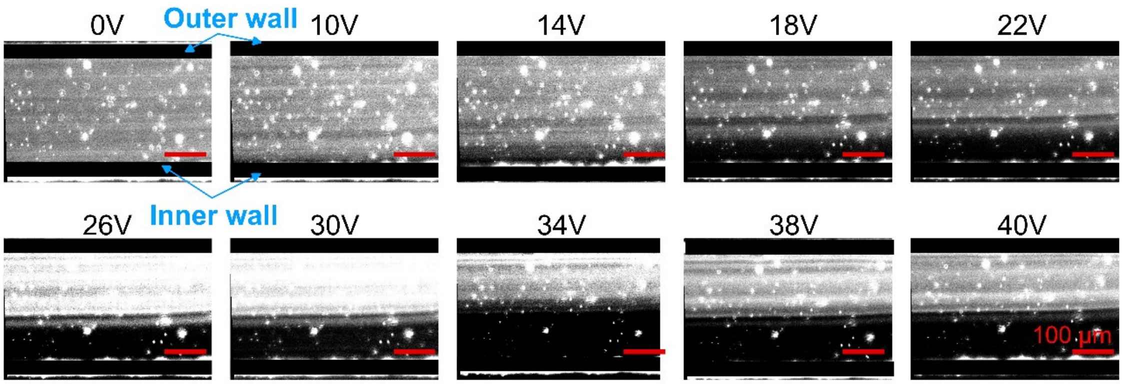

Fig. S8. The effect of the electric voltage on focusing 500-nm particles in a DEP-spiral channel. The flow rate was kept constant at 50 µL/min (Re = *9*).

Fig. S9 Focusing of 1.1 µm particles in a DEP-spiral channel.

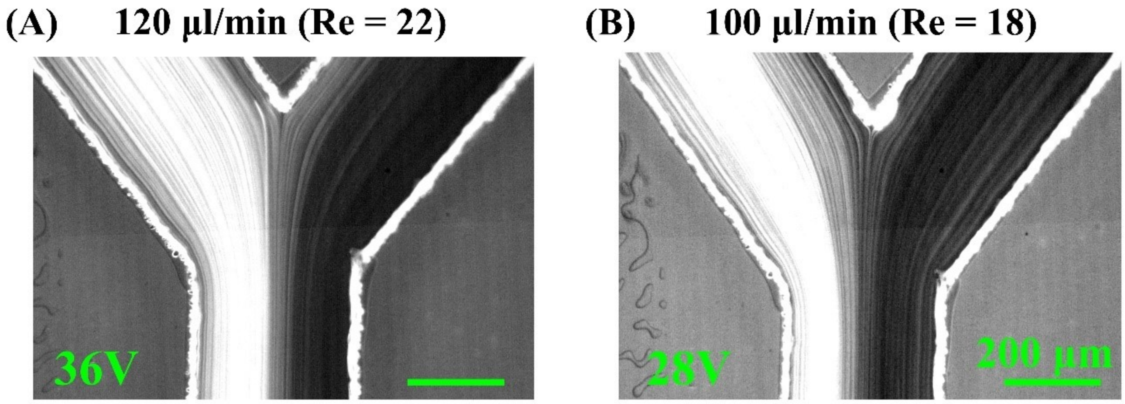

Fig. S9. Focusing of 1.1 µm particles at (A) 120 µL/min (Re = 22)and (B) 100 µL/min (Re = 18). At a higher flow rate of 120 µL/min, a large electric voltage is needed to achieve equivalent focusing of 1.1-µm particles compared to a lower flow rate (100 µL/min).

Fig. S10 Focusing behaviours of 100-nm and 200-nm polystyrene particles

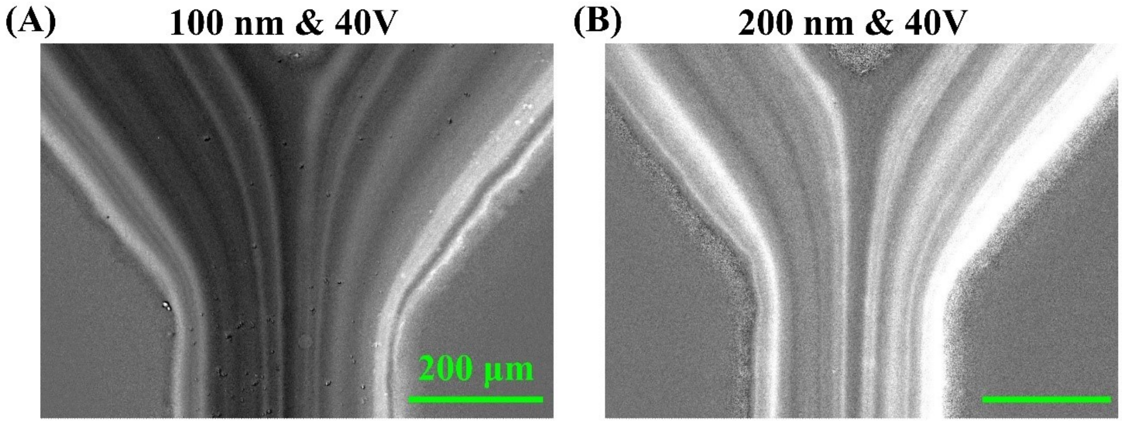

Fig. S10. The focusing of (A) 100-nm and (B) 200-nm polystyrene particles at 40 V (V_{pp}) and 50 µL/min (Re = 9). No obvious migration of particles toward one sidewall, but rather random dispersal. The potential reason is that the DEP force on smaller particles is too weak to sufficiently push particles vertically to the effective secondary flow region. We didn't test the higher electrical voltage because of the electrolysis issue of electrodes at higher voltages.

Movie S1 (separate file). Size-based separation of 8-μm and 10-μm particles.

Movie S2 (separate file). Dielectric property-based separation of live and dead CHO cells.

Movie S3 (separate file). Separation of 1.1-μm and 200-nm particles using the hybrid DEP-inertial microfluidic device. 1.1-μm particles are focused along the outer wall, while 200 nm particles are widely distributed.

SI References

1. J. Zhang, S. Yan, D. Yuan, G. Alici, N.-T. Nguyen, M. E. Warkiani and W. Li, *Lab on a Chip*, 2016, **16**, 10-34.
2. W. Tang, S. Zhu, D. Jiang, L. Zhu, J. Yang and N. Xiang, *Lab on a Chip*, 2020, **20**, 3485-3502.
3. D. Di Carlo, *Lab on a Chip*, 2009, **9**, 3038-3046.
4. H. Amini, W. Lee and D. Di Carlo, *Lab on a Chip*, 2014, **14**, 2739-2761.
5. J. Zhou and I. Papautsky, *Lab on a Chip*, 2013, **13**, 1121-1132.
6. J. Zhang, S. Yan, G. Alici, N.-T. Nguyen, D. Di Carlo and W. Li, *Rsc Advances*, 2014, **4**, 62076-62085.
7. D. Di Carlo, D. Irimia, R. G. Tompkins and M. Toner, *Proceedings of the National Academy of Sciences*, 2007, **104**, 18892-18897.
8. J. Zhang, D. Yuan, Q. Zhao, A. J. Teo, S. Yan, C. H. Ooi, W. Li and N.-T. Nguyen, *Analytical chemistry*, 2019, **91**, 4077–4084.
9. Y. Zhou, Z. Ma and Y. Ai, *Microsystems & nanoengineering*, 2018, **4**, 1-14.
10. J. Zhang, D. Yuan, Q. Zhao, A. J. Teo, S. Yan, C. H. Ooi, W. Li and N.-T. Nguyen, *Analytical chemistry*, 2019, **91**, 4077-4084.
11. E. A. Kwizera, M. Sun, A. M. White, J. Li and X. He, *ACS Biomaterials Science & Engineering*, 2021.
12. X.-B. Wang, Y. Huang, F. Becker and P. Gascoyne, *Journal of Physics D: Applied Physics*, 1994, **27**, 1571.
13. F. Yang, Y. Zhang, X. Cui, Y. Fan, Y. Xue, H. Miao and G. Li, *Biotechnology journal*, 2019, **14**, 1800181.
14. M. Alshareef, N. Metrakos, E. Juarez Perez, F. Azer, F. Yang, X. Yang and G. Wang, *Biomicrofluidics*, 2013, **7**, 011803.
15. C. Zhang, K. Khoshmanesh, A. Mitchell and K. Kalantar-Zadeh, *Analytical and bioanalytical chemistry*, 2010, **396**, 401-420.
16. N.-V. Nguyen, T. Le Manh, T. S. Nguyen, V. T. Le and N. Van Hieu, *Journal of Science: Advanced Materials and Devices*, 2021, **6**, 11-18.
17. N. Abd Rahman, F. Ibrahim and B. Yafouz, *Sensors*, 2017, **17**, 449.
18. B. J. Downey, L. J. Graham, J. F. Breit and N. K. Glutting, *Biotechnol. Prog.*, 2014, **30**, 479-487.
19. J. Zhang, D. Yuan, Q. Zhao, S. Yan, S.-Y. Tang, S. H. Tan, J. Guo, H. Xia, N.-T. Nguyen and W. Li, *Sensors and Actuators B: Chemical*, 2018, **267**, 14-25.